Proceedings of the ASME 2021
International Design Engineering Technical Conferences and
Computers and Information in Engineering Conference
IDETC/CIE2021
August 17-20, 2021, Virtual, Online

DETC2021-67317

MULTI-MATERIAL AND MULTI-JOINT TOPOLOGY OPTIMIZATION FOR LIGHTWEIGHT AND COST-EFFECTIVE DESIGN

Luke Crispo[1], Stephen William Knox Roper[1], Rubens Bohrer[1], Rosalie Morin[1], Il Yong Kim[1*]
[1]Queen's University, Kingston, ON, Canada
*kimiy@queensu.ca

ABSTRACT

Lightweighting and cost reduction are overarching research themes in aerospace and automotive industries, leading to the exploration of new materials, advanced manufacturing methods, and design optimization algorithms. Multi-material topology optimization is an important tool that can generate unconventional designs leveraging the differing mechanical properties of multiple material types to increase performance. However, these approaches do not consider joining design during optimization, which can ultimately result in higher cost, worse performance, and unrealistic designs that must be altered in the interpretation stage. This work presents a multi-material and multi-joint topology optimization methodology that models joints at the interfaces between dissimilar materials, controls the joining pattern using joint design variables, and reduces cost through the addition of a joining cost constraint. Design variable interpolation schemes, interface detection for unstructured meshes, and sensitivity analysis are outlined in detail in this paper. The approach is applied to a real-world rocker arm geometry to demonstrate the importance of considering joints during multi-material topology optimization. The results of the numerical example indicate that the methodology can successfully detect interfaces in unstructured meshes and strategically place joints to maximize stiffness of the structure. A parameter study of various joining cost constraint levels illustrates how the optimizer alters part topology and joining design to reduce cost.

Keywords: Multi-material topology optimization; multi-joint topology optimization; joint design; structural optimization

NOMENCLATURE

C	structural compliance
E_e	interpolated stiffness of the eth element
E^j	stiffness of the jth material / joint type
$\underset{\sim}{f}$	nodal applied force vector
g^1	mass fraction constraint
g^2	joining cost fraction constraint
$\underset{\sim}{K}$	global stiffness matrix
$\tilde{\eta}$	projected interface vector
p	SIMP penalty factor
$\underset{\sim}{\rho}^1$	material existence design variable vector
$\underset{\sim}{\rho}^2$	material selection design variable vector
$\underset{\sim}{\rho}^3$	joint existence design variable vector
$\underset{\sim}{\rho}^4$	joint selection design variable vector
ρ_e^j	jth design variable value of the eth element
Q_e	interpolated cost of the eth element
$\bar{Q}$	joining cost fraction constraint limit
q^j	joint cost of the jth joint type
$\underset{\sim}{u}$	nodal displacement vector
V_e	volume of the eth element
W_e	interpolated mass of the eth element
$\bar{W}$	mass fraction constraint limit
ω^j	physical density of the jth material / joint type

1. INTRODUCTION

As aerospace and automotive industries strive for lightweight and cost-effective parts, topology optimization (TO) has become an important tool for generating new design concepts [1, 2]. TO determines the ideal part geometry within a design space to maximize a specified performance metric subject

to defined constraints. Multi-material topology optimization (MMTO) is an emerging technique that extends the Solid Isotropic Material with Penalization (SIMP) interpolation scheme to simultaneously select the ideal geometry and material distribution for a component [3]. By efficiently allocating multiple materials within a design space based on their mechanical properties, MMTO can generate improved performance over single material designs [4].

The traditional MMTO problem formulation assumes that two materials can be perfectly bonded together without the need for any assembly hardware, welds, or adhesive bonds. This artificially strengthens the connection between two materials and over-predicts the stiffness of the topology optimization result. A post-processing step is also required after the optimization to translate the raw MMTO results into a realistic multi-material design with joining. Because the optimization does not consider this interpretation step, it will converge to an inferior design after accounting for joining between parts. The connections between materials also require additional assembly operations that add cost and manufacturing time compared to a single material design. Without accounting for these joining costs, MMTO algorithms fail to consider an important design criterion and will generate more expensive designs that are less likely to be implemented in industry.

Multi-material and multi-joint topology optimization (MM-MJ TO) addresses these limitations by modelling joints at the interfaces between dissimilar materials [5]. Current MM-MJ TO approaches detect interfaces using a Sobel operator calculation that can only be applied to uniformly structured hexahedral finite element (FE) meshes, limiting the application of the methodology to academic problems [6]. The objective of this work is to present the fundamental theory for multi-material and multi-joint topology optimization and to develop a novel approach that can be applied to an unstructured FE mesh. The effectiveness of the methodology will be demonstrated by solving a verification problem with realistic 3D geometry.

2. METHODOLOGY

2.1 Problem Statement

The TO problem statement to be solved by the MM-MJ algorithm is outlined in (1), where the objective function is to minimize the structural compliance, $C(\underset{\sim}{\rho}^j)$, subject to a mass fraction constraint $g^1(\underset{\sim}{\rho}^j)$ and joining cost fraction constraint $g^2(\underset{\sim}{\rho}^m)$. The geometry of the structure is determined using four continuous design variable fields. Similar to the standard MMTO approach, $\underset{\sim}{\rho}^1$ and $\underset{\sim}{\rho}^2$ determine the existence of material within the design domain and select the material type (material 1 or material 2), respectively. These are accompanied by joining design variables $\underset{\sim}{\rho}^3$ and $\underset{\sim}{\rho}^4$, which respectively determine joint existence and select joint type (joint type 1 or joint type 2).

$$\begin{aligned} \underset{\underset{\sim}{\rho}^1,\underset{\sim}{\rho}^2,\underset{\sim}{\rho}^3,\underset{\sim}{\rho}^4}{\text{minimize}} \quad & C\left(\underset{\sim}{\rho}^j\right) = \underset{\sim}{u}^T \underline{\underline{K}}\,\underset{\sim}{u} \\ \text{subject to} \quad & \underline{\underline{K}}\,\underset{\sim}{u} = \underset{\sim}{f} \\ & \mathrm{g}^1\left(\underset{\sim}{\rho}^j\right) = \sum W_e \;/\; \sum \omega^1 V_e \;\le \bar{W} \\ & \mathrm{g}^2\left(\underset{\sim}{\rho}^m\right) = \sum Q_e \;/\; \sum V_e \;\le \bar{Q} \\ & \forall \text{ element } e,\ \rho_e^j \in (0,1],\ j = 1,2,3,4 \\ & \qquad\qquad \rho_e^m \in (0,1],\ m = 2,3,4 \end{aligned} \tag{1}$$

The geometry is subject to a linear static governing equation, where $\underline{\underline{K}}(\underset{\sim}{\rho}^j)$ is the global stiffness matrix, $\underset{\sim}{u}\left(\underset{\sim}{\rho}^j\right)$ is the vector of nodal displacements, and $\underset{\sim}{f}$ is the vector of applied loads. The mass fraction constraint ensures that the weight of the structure stays below a specified limit $\bar{W}$ and the joining cost fraction constraint limits the joining cost below $\bar{Q}$, defined as the ratio of joining cost to the total volume of the structure. $W_e(\rho_e^j)$ and $Q_e(\rho_e^m)$ are the interpolated mass and joining cost of the eth element, respectively, while ω^1 is the physical density of the stiffest material and V_e is the elemental volume.

2.2 Element Interpolation Schemes

Density-based TO approaches interpolate the properties of an element based on design variable values. The standard multi-material interpolation equations for two materials are outlined in (2) and (3), where $E_e(\rho_e^1, \rho_e^2)$ is the Young's modulus of the eth element used to generate the element's stiffness matrix. Based on this equation, a design variable value of $\rho_e^1 = 0$ corresponds to void, while $\rho_e^1 = 1$ and $\rho_e^2 = 1$ corresponds to material 1 (with a stiffness of E^1 and physical density of ω^1) and $\rho_e^1 = 1$ and $\rho_e^2 = 0$ corresponds to material 2 (with a stiffness of E^2 and physical density of ω^2). A SIMP penalty factor p is introduced on both design variables in the stiffness interpolation to discourage intermediate density elements.

$$E_e\left(\rho_e^1, \rho_e^2\right) = \left(\rho_e^1\right)^p \left(\left(\rho_e^2\right)^p E^1 + \left(1 - \left(\rho_e^2\right)^p\right) E^2\right) \tag{2}$$

$$W_e\left(\rho_e^1, \rho_e^2\right) = \rho_e^1 \left(\rho_e^2 \omega^1 + \left(1 - \rho_e^2\right)\omega^2\right) V_e \tag{3}$$

The MM-MJ interpolation scheme for element stiffness in (4) uses a projected interface term, $\tilde{n}_e$, that is formulated to have a value of unity for elements that lay on the interface between dissimilar materials and a value of zero otherwise. Therefore, for elements that do not exist on the material interface, (4) is equal to original MMTO interpolation in (2). When $\tilde{n}_e = 1$, the MM-MJ interpolation becomes a function of the joining design variables $\underset{\sim}{\rho}^3$ and $\underset{\sim}{\rho}^4$, and joint stiffnesses E^3 and E^4. All design variables are penalized using the same penalty factor p.

$$\begin{aligned} E_e\left(\rho_e^j\right) = {} & \left(1 - \tilde{n}_e\right)\left(\rho_e^1\right)^p \left(\left(\rho_e^2\right)^p E^1 + \left(1 - \left(\rho_e^2\right)^p\right) E^2\right) \\ & + \tilde{n}_e \left(\rho_e^3\right)^p \left(\left(\rho_e^4\right)^p E^3 + \left(1 - \left(\rho_e^4\right)^p\right) E^4\right) \end{aligned} \tag{4}$$

An element's interpolated mass is calculated in a similar fashion in (5), using the respective material and joint physical densities ω^j. Design variable penalization is not applied to the mass interpolation equation.

$$W_e\left(\rho_e^j\right) = \left(1-\tilde{n}_e\right)\rho_e^1\left(\rho_e^2\omega^1 + \left(1-\rho_e^2\right)\omega^2\right)V_e + \tilde{n}_e\rho_e^3\left(\rho_e^4\omega^3 + \left(1-\rho_e^4\right)\omega^4\right)V_e \tag{5}$$

The joining cost of an element is approximated by (6) for interface elements as an interpolation between q^3 and q^4, the unit cost per volume assigned to joint type 1 and joint type 2, respectively. It is important to note that while joint cost is presented in dollars, this joining cost term is a pseudo-cost measure that only considers the relative difference in cost between two joining methods. This approach does not attempt to calculate the true joining cost of an assembly, which is a complex relationship involving parameters such as material costs, tooling accessibility, labour, and heat treatment/curing costs, to name a few.

$$Q_e\left(\rho_e^m\right) = \tilde{n}_e\rho_e^3\left(\rho_e^4 q^3 + \left(1-\rho_e^4\right)q^4\right)V_e \tag{6}$$

2.3 Interface Detection

The interface term presented in (4) - (6) is calculated using the spatial gradient of the material selection design variable $(\underset{\sim}{\rho}^2)$. The spatial gradient calculation determines where the density field changes from $\rho_e^2 = 1$ to $\rho_e^2 = 0$, indicating elements on the boundary of material 1. This work uses the spatial gradient interface detection methodology developed by Crispo et al. as it can be applied to any unstructured FE mesh [7]. The spatial gradient in the *k*th direction of the penalized material selection design variable, $\nabla_k\rho_e^2$, is calculated in (7). Both summations are computed over N neighbouring elements within a search radius r about the *e*th element. A radius of 2X the average mesh size was used in this work for spatial gradient calculations. The distance term H_i in (8) decreases in magnitude as the distance from the central element increases. The $\cos\theta_{k,i}$ term calculates the cosine of the angle between the unit vector in the *k*th direction and the vector from the *e*th element to the *i*th neighbouring element.

$$\nabla_k\rho_e^2 = \frac{\sum_{i=1}^{N} H_i V_i\left(\rho_i^2\right)^p \cos\theta_{k,i}}{\sum_{i=1}^{N} H_i V_i}, \qquad k = 1,2,3 \tag{7}$$

$$H_i = \max\left\{0, r - \text{distance}\left(e,i\right)\right\} \tag{8}$$

A spatial gradient vector can be formed from each of the *k*th directional components of the spatial gradient. The magnitude of this vector, n_e calculated in (9), is an indicator of the interface of material 1.

$$n_e = \left\|\nabla\rho_e^2\right\| = \sqrt{\sum_{k=1}^{3}\left(\nabla_k\rho_e^2\right)^2}, \tag{9}$$

The spatial gradient magnitude then goes through a thinning and Heaviside projection operation to ultimately yield the interface term used in the MM-MJ interpolation schemes. The thinning calculation in (10) removes interface values in solid elements, while the projection scheme in (11) results in near discrete interface values. The projection parameters β and η adjust the slope and horizontal shift of the function, respectively. Values of $\beta = 70$ and $\eta = 0.02$ were used in this work.

$$\hat{n}_e = \left(1-\rho_e^2\right)n_e \tag{10}$$

$$\tilde{n}_e = \frac{1}{1+e^{-2\beta\left(\hat{n}_e-\eta\right)}} \tag{11}$$

2.4 Sensitivity Analysis

The MM-MJ TO approach uses a gradient based optimizer that requires sensitivity information of the objective and constraint functions with respect to each design variable. These sensitivities are derived analytically and calculated each iteration of the optimization. The objective and constraint sensitivities of the $j = 1,3,4$ design variable fields are outlined in (12) - (14). Readers are referred to [8] for a detailed derivation of the compliance sensitivity expression using the adjoint variable method. The elemental compliance C_e can be obtained as a direct output from most FE solvers.

$$\frac{dC}{d\rho_e^j} = -\frac{C_e}{E_e}\frac{\partial E_e}{\partial\rho_e^j}, \qquad j = 1,3,4 \tag{12}$$

$$\frac{dg^1}{d\rho_e^j} = \frac{1}{\sum\omega^1 V_e}\frac{\partial W_e}{\partial\rho_e^j}, \qquad j = 1,3,4 \tag{13}$$

$$\frac{dg^2}{d\rho_e^j} = \frac{1}{\sum V_e}\frac{\partial Q_e}{\partial\rho_e^j}, \qquad j = 1,3,4 \tag{14}$$

The sensitivities with respect to the material selection design variable field ($\underset{\sim}{\rho}^2$) must be modified to account for the effect that the N neighboring element's material selection design variable has on the *e*th element's interface term. The chain rule derivation obtains the sensitivities in (15) - (17). These equations include the effect that any given *e*th element's material selection design variable has on its own properties, as well as its effect on the interfaces (and therefore properties) of the surrounding *i*th elements.

$$\frac{dC}{d\rho_e^2} = -\frac{C_e}{E_e}\frac{\partial E_e}{\partial\rho_e^2} - \sum_{i=1}^{N}\frac{C_i}{E_i}\frac{\partial E_i}{\partial\rho_e^2} \tag{15}$$

$$\frac{dg^1}{d\rho_e^2} = \frac{1}{\sum\omega^1 V_e}\left(\frac{\partial W_e}{\partial\rho_e^2} + \sum_{i=1}^{N}\frac{\partial W_i}{\partial\rho_e^2}\right) \tag{16}$$

$$\frac{dg^2}{d\rho_e^2} = \frac{1}{\sum V_e}\left(\frac{\partial Q_e}{\partial \rho_e^2} + \sum_{i=1}^{N}\frac{\partial Q_i}{\partial \rho_e^2}\right) \tag{17}$$

The sensitivities of the interpolation equations for stiffness ($\partial E_e / \partial \rho_e^j$), mass ($\partial W_e / \partial \rho_e^j$), and cost ($\partial Q_e / \partial \rho_e^j$) in the MM-MJ formulation are outlined in [6], however the sensitivity of the *e*th interface term with respect to the *e*th central element is modified as shown in (18). These terms can be back substituted into (12) - (14) to calculate the sensitivities of the $j = 1,3,4$ design variable fields. It should be noted that when deriving the interface sensitivities, the derivative of the spatial gradient $\partial n_e / \partial \rho_e^2$ is equal to zero because the central element is not included in the summation of (7).

$$\frac{\partial \tilde{n}_e}{\partial \rho_e^2} = -n_e \frac{2\beta e^{-2\beta(\hat{n}_e - \eta)}}{\left(1 + e^{-2\beta(\hat{n}_e - \eta)}\right)^2} \tag{18}$$

The sensitivity expressions of the *i*th element's interpolation equations with respect to the *e*th element's material selection design variable are outlined in (19) - (21). These equations are obtained through direct differentiation of (4) - (6) after substituting subscript *i* for *e*, and noting that the *i*th interface term $\tilde{n}_i\left(\underset{\sim}{\rho}^2\right)$ is a function of its neighbouring elements.

$$\begin{aligned}\frac{\partial E_i}{\partial \rho_e^2} = &-\frac{\partial \tilde{n}_i}{\partial \rho_e^2}\left(\rho_i^1\right)^p\left(\left(\rho_i^2\right)^p E^1 + \left(1-\left(\rho_i^2\right)^p\right)E^2\right) \\ &+\frac{\partial \tilde{n}_i}{\partial \rho_e^2}\left(\rho_i^3\right)^p\left(\left(\rho_i^4\right)^p E^3 + \left(1-\left(\rho_i^4\right)^p\right)E^4\right)\end{aligned} \tag{19}$$

$$\begin{aligned}\frac{\partial W_i}{\partial \rho_e^2} = &-\frac{\partial \tilde{n}_i}{\partial \rho_e^2}\rho_i^1\left(\rho_i^2\omega^1 + \left(1-\rho_i^2\right)\omega^2\right)V_i \\ &+\frac{\partial \tilde{n}_i}{\partial \rho_e^2}\rho_i^3\left(\rho_i^4\omega^3 + \left(1-\rho_i^4\right)\omega^4\right)V_i\end{aligned} \tag{20}$$

$$\frac{\partial Q_i}{\partial \rho_e^2} = \frac{\partial \tilde{n}_i}{\partial \rho_e^2}\rho_i^3\left(\rho_i^4 q^3 + \left(1-\rho_i^4\right)q^4\right)V_i \tag{21}$$

The final sensitivity derivation needed is the $\partial \tilde{n}_i / \partial \rho_e^2$ term that determines the impact of the *e*th element's material selection design variable on the *i*th neighbour's interface term. Direct differentiation of the thresholding and thinning step in (10) and (11) for the *i*th element yields (22).

$$\frac{\partial \tilde{n}_i}{\partial \rho_e^2} = \left(1-\rho_i^2\right)\frac{2\beta e^{-2\beta(\hat{n}_i - \eta)}}{\left(1 + e^{-2\beta(\hat{n}_i - \eta)}\right)^2}\frac{\partial n_i}{\partial \rho_e^2} \tag{22}$$

The spatial gradient sensitivity can be expressed through differentiation of (7) and (9) for the *i*th element, resulting in

$$\frac{\partial n_i}{\partial \rho_e^2} = \frac{H_e V_e p\left(\rho_e^2\right)^{(p-1)}}{n_i \sum_{i=1}^{N} H_i V_i}\sum_{k=1}^{3}\left(\left(\nabla_k \rho_i^2\right)\cos\theta_{k,e}\right). \tag{23}$$

These terms can then be back substituted through to (15) - (17) for the $j = 2$ design variable field for use in the gradient based optimizer.

2.5 Filtering

Density-based TO approaches require a filtering technique to avoid checkerboarding patterns. This work uses the mesh independent filter from Sigmund, which filters the sensitivities using a search radius about the central element [9]. A generic sensitivity $\partial \Phi / \partial \rho_e^j$ is filtered as

$$\left(\frac{\partial \Phi}{\partial \rho_e^j}\right)^* = \frac{1}{\rho_e^j / V_e \sum_{i=1}^{N} H_i}\sum_{i=1}^{N}\left(H_i \rho_i^j \frac{\partial \Phi}{\partial \rho_i^j} / V_i\right), \tag{24}$$

where H_i is the distance term from (8) and the filtered sensitivity is denoted by an asterisk. A neighbourhood search radius of 1.5× the average mesh size was used for the sensitivity filtering and the central element was included in the summation term.

3. NUMERICAL EXAMPLE

The capability of the proposed MM-MJ TO methodology is demonstrated on a simplified rocker arm structure. First the advantages of multi-material design will be explored, followed by an investigation into the effect of modelling joints in the optimization and using a cost constraint to alter the joining design. The FE model of the geometry to be optimized is shown in Fig. 1 with the design space in green and the non-designable regions in grey. This model contains a solid 3D mapped mesh of hexahedral and pentahedral elements, with a total of 36,810 designable elements. The FE model contains three load cases outlined in Fig. 2 with a single load of 1000 N applied in each load case. The constrained degrees of freedom are also indicated in Fig. 2. All loads and single point constraints are applied to nodes in the center of each cylinder that are attached using RBE2 elements to the inside faces of each cylinder.

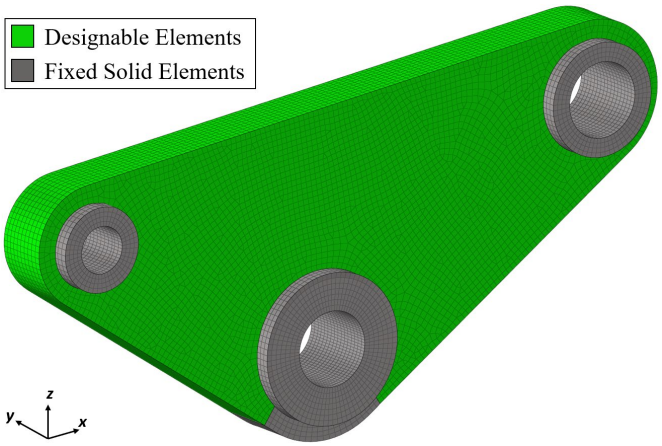

FIGURE 1: FINITE ELEMENT MODEL OF ROCKER ARM DESIGN AND NON-DESIGN SPACE

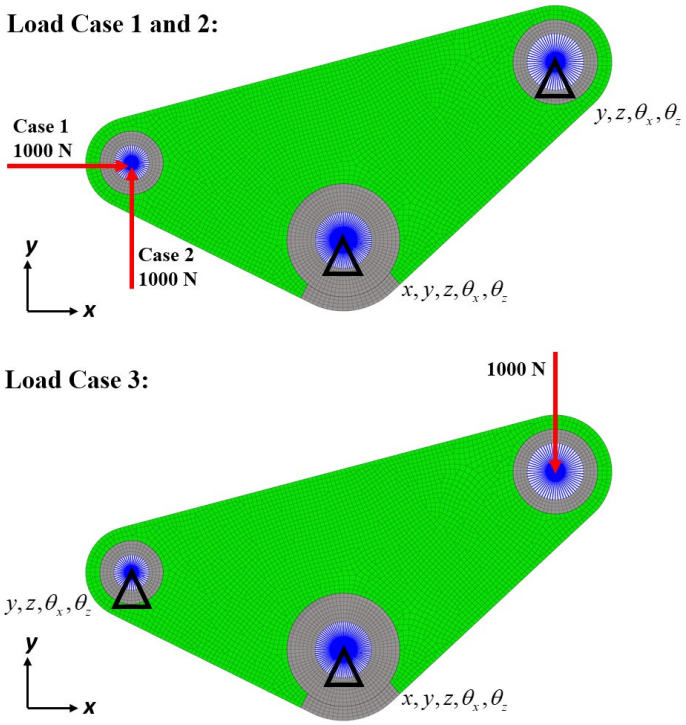

FIGURE 2: LOAD CASES AND BOUNDARY CONDITIONS OF THE ROCKER ARM MODEL

The MM-MJ TO problem is solved using an in-house solver that interfaces with Altair OptiStruct for FE analysis. The custom topology optimization tool uses the gradient-based Method of Moving Asymptotes (MMA) to iteratively solve the optimization problem statement in a three-phase convergence scheme [10]. The optimization was solved using a Windows PC (Ryzen 9 3950X, 16 cores @ 3.5 GHz, 128 GB RAM) with computational times ranging between 1 – 2 hours.

The multi-material algorithm was provided with the option of selecting titanium or aluminum within the design space. The material stiffness and densities are listed in Table 1, while the Poisson's ratio was fixed at 0.355. The mechanical properties of the weld were calculated as an average of both materials, while those of the adhesive were calculated using an average with a weakening factor to reduce the stiffness. The averaging approach was used because the true thickness of the joint would be smaller than the average element size in the model. It is acknowledged that these joining properties are somewhat arbitrary, however they are sufficient to assess the capability of the methodology. The joining cost of the weld was arbitrarily set as double the cost of an adhesive bond. Material cost is not considered in this approach.

TABLE 1: MATERIAL PROPERTIES AND JOINT COSTS OF DESIGNABLE MATERIALS

Material Property	Titanium	Aluminum	Weld	Adhesive
Stiffness (E) [GPa]	110	70	82	27
Density (ω) [g/cm^3]	4.50	2.70	3.6	2.88
Joint Cost (q) [\$/cm^3]	N/A	N/A	2	1

3.1 Multi-Material Topology Optimization

To demonstrate the advantages of using multiple materials in structural design, the rocker arm geometry was first optimized using a single-material formulation for both titanium and aluminum, respectively. A MMTO solution considering both titanium and aluminum was completed for comparison. All studies used a 50% mass fraction constraint relative to a solid titanium design space. No joint cost constraint was implemented as joining was not considered at this stage. Fig. 3 shows the density contour results for the three problem statements with each material shown in a different colour and void elements removed. The multi-material solution places the stiffer material in the main load paths of the structure to obtain a 5.8% reduction in compliance over the titanium design and a 9.2% reduction over the aluminum design. All optimizations resulted in an equivalent mass of 2.51 kg.

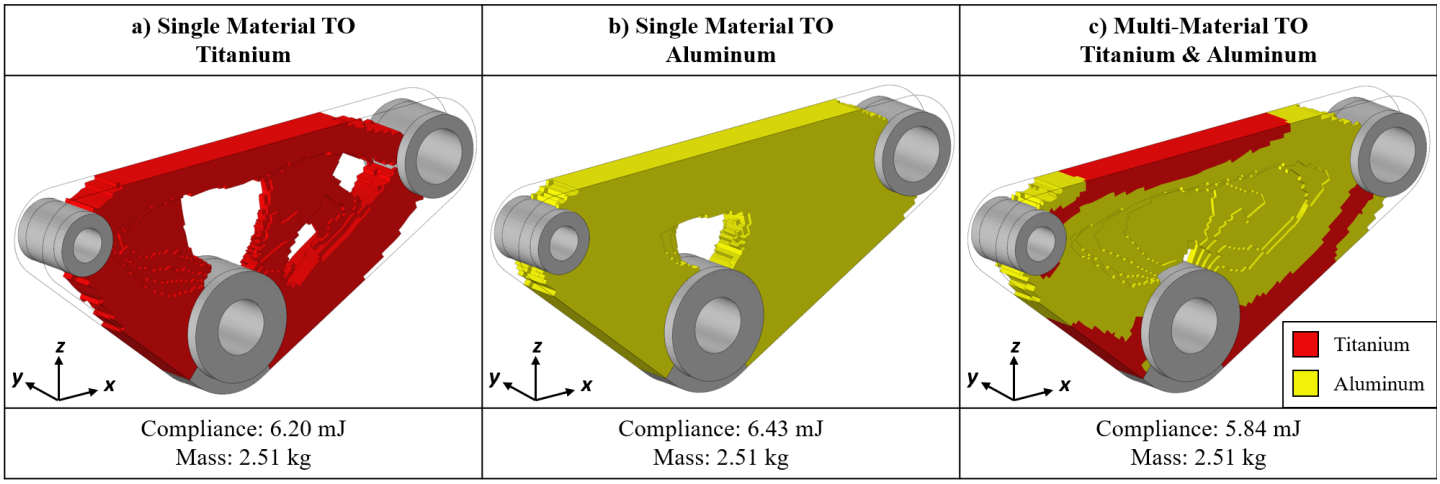

FIGURE 3: SINGLE AND MULTI-MATERIAL TOPOLOGY OPTIMIZATION RESULTS

It is important to note that while the multi-material design yielded a performance improvement, the stiffness of the joints between dissimilar materials was not accounted for. This artificially stiffened the MMTO design, overpredicting real-world performance. In addition, the optimizer generated some small titanium and aluminum features that would be impractical to implement and would typically be removed during a design interpretation phase. To address these concerns, the MM-MJ-TO methodology must be implemented to model and optimize the joint design.

3.2 Multi-Material Multi-Joint Topology Optimization

The rocker arm geometry was then solved using the MM-MJ TO problem statement without a joint cost constraint. In this setup, the optimizer placed as many joints as possible to maximize stiffness. Results from this optimization shown in Fig. 4 b) indicate that the approach accurately calculated the interface of the titanium geometry and placed the stiffer welds at all interfaces. The placement of titanium within the design space was similar to the MMTO solution, however the compliance increased by 2.4% due to the introduction of joints. The MM-MJ TO solution also predicted a joining cost that was not considered in the traditional multi-material result. A limitation of this approach is evident in Fig. 4 b) where some joints were placed at the interface of titanium to void. This occurred because the approach calculates the boundary of the titanium geometry, which is not exactly equivalent to the interface between the two materials.

In Fig. 4 c), a joint cost constraint of 5% was added to the problem statement. This result altered the placement of titanium within the design space to reduce the joining cost, albeit with an increase in compliance. This solution reduced joining cost by 63% over the baseline MM-MJ result with a 1.5% increase in compliance. Both MM-MJ TO results achieved a lower compliance compared to the single material TO results.

The effect of the joining cost constraint was further investigated by optimizing the rocker arm design for cost constraints ranging from 13% to 3%. Fig. 5 displays a Pareto frontier of the optimized designs in terms of compliance and joining cost, which were normalized relative to the baseline single material design in Fig. 3 a) and the baseline MM-MJ TO design in Fig. 4 b), respectively. All designs except for the 3% cost constraint obtained a lower compliance than the single material result. As the joint cost constraint was tightened, the optimizer gradually removed the smaller titanium features. Below a cost constraint of 7%, the material layout remained constant while welds along the interface were gradually removed at non-critical locations. This reduced joining cost but may have other implications on stress, which was not studied in this work. Adhesives were used sparingly in all designs due to their inferior mechanical properties and only began to appear at cost fraction constraints below 4%. Further investigation should be conducted to determine if the optimization parameters have an impact the use of adhesives in the optimized result. At the lowest cost fraction constraint, the MM-MJ-TO solution resulted in worse compliance compared to the single part design, indicating that multi-material parts may have worse performance when the connection area is significantly reduced.

A checkerboarding effect was observed in localized interface regions in severely joint cost constrained designs, however this effect is not pictured in this work and was corrected with a manual post-processing step for the figures displayed. A filtering calculation could be implemented on the interface term as the design variable sensitivity filtering in this work was insufficient to prevent interface checkerboarding. It should also be noted that while some materials appear to be directly connected in Fig. 4 c) and Fig. 5, this is because only a single view is presented of a complex 3D geometry.

4. CONCLUSION

This paper presents a detailed methodology for multi-material and multi-joint topology optimization of unstructured finite element meshes. The capability of the approach was demonstrated on a practical 3D geometry for a variety of

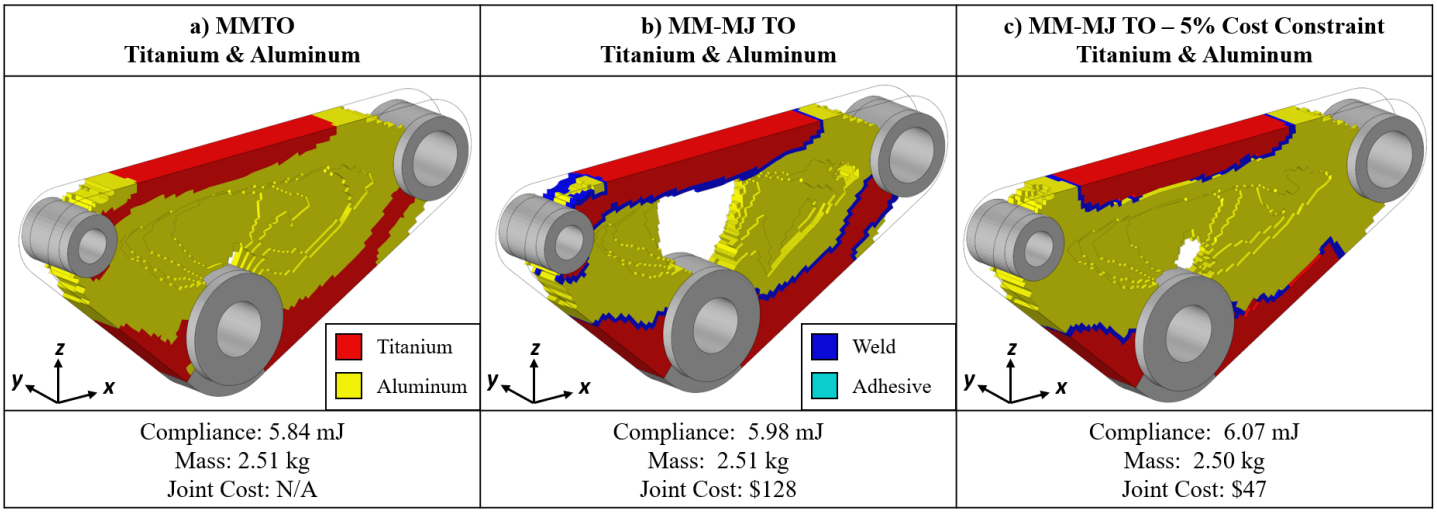

FIGURE 4: MULTI-MATERIAL AND MULTI-JOINT TOPOLOGY OPTIMIZATION RESULTS

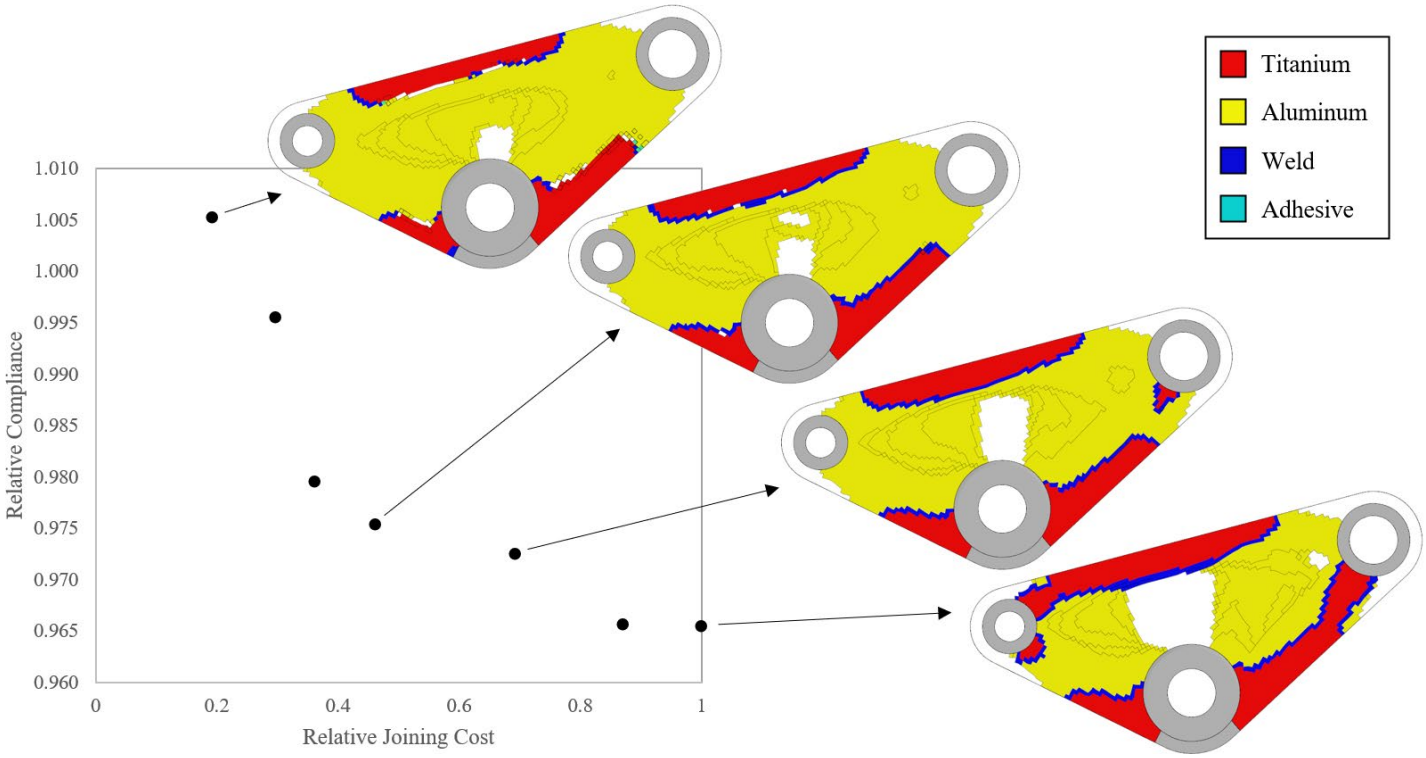

FIGURE 5: PARETO FRONTIER OF COMPLIANCE AND JOINING COST FOR THE MULTI-JOINT PROBLEM STATEMENT WITH VARYING JOINT COST CONSTRAINTS

problem statements. Results indicated that the algorithm can effectively change the material and joint distribution to reduce joining cost while decreasing compliance over single material designs. Future work includes refinement of the interface calculation near void areas and to improve checkerboarding at low joining cost constraints. In addition, the joining between non-designable regions and the design space was not considered in this work. There are also many important joining factors that should ultimately be implemented in MM-MJ TO, such as tooling accessibility, galvanic corrosion, heat affected zones, and joint failure models.

REFERENCES

[1] Zhu, J. H., Zhang, W. H., and Xia, L. "Topology Optimization in Aircraft and Aerospace Structures Design." *Archives of Computational Methods in Engineering* Vol. 23 No. 4 (2016): pp. 595-622. DOI 10.1007/s11831-015-9151-2.

[2] Li, C., Kim, I. Y., and Jeswiet, J. "Conceptual and detailed design of an automotive engine cradle by using topology, shape, and size optimization." *Structural and Multidisciplinary Optimization* Vol. 51 No. 2 (2015): pp. 547-564. DOI 10.1007/s00158-014-1151-6.

[3] Bendsoe, M. P. and Sigmund, O. *Topology Optimization: Theory, Methods, and Applications.* Springer Berlin Heidelberg (2003).

[4] Li, D. and Kim, I. Y. "Multi-material topology optimization for practical lightweight design." *Structural and Multidisciplinary Optimization* Vol. 58 No. 3 (2018): pp. 1081-1094. DOI 10.1007/s00158-018-1953-z.

[5] Woischwill, C. and Kim, I. Y. "Multimaterial multijoint topology optimization." *International Journal for Numerical Methods in Engineering* Vol. 115 No. 13 (2018): pp. 1552-1579. DOI 10.1002/nme.5908.

[6] Florea, V., Pamwar, M., Sangha, B., and Kim, I. Y. "Simultaneous single-loop multimaterial and multijoint topology optimization." *International Journal for Numerical Methods in Engineering* Vol. 121 No. 7 (2020): pp. 1558-1594. DOI 10.1002/nme.6279.

[7] Crispo, L., Bohrer, R., Roper, S. W. K., and Kim, I. Y. "Spatial gradient interface detection in topology optimization for an unstructured mesh." *Structural and Multidisciplinary Optimization* Vol. 63 (2021): pp. 515-522. DOI 10.1007/s00158-020-02688-z.

[8] Roper, S., Vierhout, G., Li, D., Sangha, B., Pamwar, M., and Kim, I. Y. "Multi-Material Topology Optimization and Multi-Material Selection in Design." *WCX SAE World Congress Experience*. 2019-01-0843: pp. 1-12. Detroit, MI, 2019. DOI 10.4271/2019-01-0843.

[9] Sigmund, O. "Morphology-based black and white filters for topology optimization." *Structural and Multidisciplinary Optimization* Vol. 33 (2007): pp. 401-424. DOI 10.1007/s00158-006-0087-x.

[10] Svanberg, K. "The Method of Moving Asymptotes - a New Method for Structural Optimization." *International Journal for Numerical Methods in Engineering* Vol. 24 No. 2 (1987): pp. 359-373. DOI 10.1002/nme.1620240207.